

Heterointerface effects on lithium-induced phase transitions in intercalated MoS₂

Sajad Yazdani^{1,2,†}, Joshua V. Pondick^{1,2,†}, Aakash Kumar^{1,2}, Milad Yarali^{1,2}, John M. Woods^{1,2}, David J. Hynek^{1,2}, Diana Y. Qiu^{1,2}, Judy J. Cha^{1,2*}

¹Department of Mechanical Engineering and Materials Science, Yale University, New Haven, CT 06511, USA.

²Energy Sciences Institute, Yale West Campus, West Haven, CT 06516, USA.

[†]These authors contributed equally.

*Correspondence to: judy.cha@yale.edu

Abstract

The intercalation-induced phase transition of MoS₂ from the semiconducting 2H to the semimetallic 1T' phase has been studied in detail for nearly a decade; however, the effects of a heterointerface between MoS₂ and other two-dimensional (2D) crystals on the phase transition have largely been overlooked. Here, *ab initio* calculations show that intercalating Li at a MoS₂-hexagonal boron nitride (*h*BN) interface stabilizes the 1T phase over the 2H phase of MoS₂ by $\sim 100 \text{ mJ m}^{-2}$, suggesting that encapsulating MoS₂ with *h*BN may lower the electrochemical energy needed for the intercalation-induced phase transition. However, *in situ* Raman spectroscopy of *h*BN-MoS₂-*h*BN heterostructures during electrochemical intercalation of Li⁺ shows that the phase transition occurs at the same applied voltage for the heterostructure as for bare MoS₂. We hypothesize that the predicted thermodynamic stabilization of the 1T'-MoS₂-*h*BN interface is counteracted by an energy barrier to the phase transition imposed by the steric hindrance of the heterointerface. The phase transition occurs at lower applied voltages upon heating the heterostructure, which supports our hypothesis. Our study highlights that interfacial effects of 2D heterostructures can go beyond modulating electrical properties and can modify electrochemical and phase transition behaviors.

Main Text

Van der Waals heterostructures comprised of different two-dimensional (2D) materials^{1,2} can exhibit novel electronic and optical properties³⁻⁵, in which the effect of heterointerfaces is important. Heterointerfaces may also play a central role in determining electrochemical properties and phase transitions of 2D materials. For MoS₂, intercalation of alkali metal ions such as Li⁺ into

the van der Waals gaps between the layers can induce a phase transition from the semiconducting trigonal prismatic 2H phase to the semimetallic octahedral 1T phase^{6–8}, followed by an additional phase transition to the distorted 1T' phase, through electron doping by the intercalants^{9–12}. The intercalation-induced phase transition has proven important for energy applications^{13–17}, and the thermodynamics of the electrochemical intercalation of Li⁺ in MoS₂ has been well-characterized^{18–20}. Despite the extensive investigation and many applications of the intercalation-induced phase transition, the effect of a heterointerface on this process has largely been overlooked.

Herein, we investigate heterointerface effects on the intercalation-induced phase transition of MoS₂ by interfacing MoS₂ with hexagonal boron nitride (*h*BN). First, *ab initio* calculations indicate that the 1T-MoS₂-*h*BN interface is thermodynamically more stable than the 2H-MoS₂-*h*BN interface when Li is inserted at the interface, suggesting that interfacing MoS₂ with *h*BN could lower the thermodynamic energy barrier for the phase transition. Second, we performed electrochemical lithium intercalation on *h*BN-MoS₂-*h*BN heterostructures using electrochemical microreactors^{20–26} and studied the intercalation-induced phase change via Raman spectroscopy, *in situ*. In contrast to the *ab initio* results, we observe that the phase transition for *h*BN-MoS₂-*h*BN heterostructures occurs at the same applied electrochemical voltage as bare MoS₂ irrespective of the Li⁺ intercalation pathways. Thus, we hypothesize that the phase transition in Li-intercalated *h*BN-MoS₂-*h*BN heterostructures is influenced by steric hindrance imposed by the heterointerface, which would counteract the predicted stabilization of the 1T-MoS₂-*h*BN interface over the 2H-MoS₂-*h*BN interface. *In situ* heating of the heterostructure during intercalation allowed for the phase transition to occur at a lower applied electrochemical voltage, supporting the hypothesis that the heterointerface imposes a barrier to intercalation. Lastly, we demonstrate that the basal planes of commercial *h*BN are ionically conductive for Li⁺.

Results

Ab initio calculations of the MoS₂-*h*BN interface with Li⁺ intercalation

We performed density functional theory (DFT) calculations to investigate the energetics of the 2H to 1T phase transition of MoS₂ in the presence and absence of an *h*BN interface (see Methods). We note that the high symmetry 1T structure was used instead of the distorted 1T' structure to reduce computational cost and because 1T is an intermediate state in the 2H to 1T' phase transition. In the absence of *h*BN, the 2H to 1T phase transition in MoS₂ is thermodynamically driven, with the 1T phase becoming more favorable (lower in energy) than the 2H phase when bulk MoS₂ is doped above -1.3 electrons per monolayer formula unit (f.u.) (Fig. 1a), consistent with previous calculations^{27,28}. In the presence of an *h*BN interface, in which monolayer MoS₂ is encapsulated by 6-layer *h*BN (Fig. 1b), the binding energy of the *h*BN-MoS₂ interface is lower for 1T-MoS₂ than for 2H-MoS₂ by ~100 mJ m⁻² when a Li atom is intercalated in the van der Waals gap between MoS₂ and *h*BN (Table 1 and see Methods for the heterostructure supercell and details of relaxation). The significant decrease in the interfacial energy for 1T-MoS₂-*h*BN over 2H-MoS₂-*h*BN with Li intercalated at the interface suggests that the nucleation barrier for the intercalation-induced phase transition would be lower for *h*BN-MoS₂-*h*BN heterostructures than for bare MoS₂.

We also considered in-plane strain due to the lattice mismatch between MoS₂ and *h*BN, which may influence the calculated stability of the 2H- and 1T-MoS₂-*h*BN interface. To create a commensurate 3x3 MoS₂-4x4 *h*BN supercell, we applied an in-plane strain of roughly 4% to *h*BN, but this strain can be reduced to about 2% by utilizing a larger 4x4 MoS₂-5x5 *h*BN supercell. However, the calculated binding energies of the two interfaces did not change in these two strain

states (Supplementary Table 1), so we conclude that the in-plane strain on *h*BN did not have an effect on the increased stability of the intercalated 1T-MoS₂-*h*BN interface.

Intercalated Li may donate charge to *h*BN at the MoS₂-*h*BN interface, which may reduce the effective doping of MoS₂. To quantify this doping, we calculated the amount of charge transfer from an intercalated Li atom to the adjacent MoS₂ and *h*BN layers. Figure 1c shows the isosurface of the charge density with a Li atom in the van der Waals gap of 2H-MoS₂-*h*BN, which shows that the majority of the charge is donated to the three S atoms that are the nearest neighbor of the Li. Some charge is also donated to the N atoms of *h*BN closest to Li (Supplementary Fig. 1). Bader charge analysis²⁹ shows that the total charge donated to the three S atoms is -0.97 electron for a freestanding monolayer of 2H-MoS₂ and is reduced to -0.87 electron in the presence of *h*BN with about -0.1 electron donated to N atoms of *h*BN (Fig. 1d). Notably, the amount of charge transfer falls off rapidly with increasing distance from the Li, with > 90% of the charge transfer confined within the ring of nearest neighbor atoms (Supplementary Fig. 1). Thus, the intercalated Li at the MoS₂-*h*BN interface still dopes MoS₂ strongly and contributes to the overall electron doping required for the phase transition of MoS₂. We therefore predict that the critical electron density and, by extension, lithium concentration required to induce the phase transition, would either be similar or even lowered by interfacing MoS₂ with *h*BN, given the lower binding energy of 1T-MoS₂-*h*BN interface.

Electrochemical intercalation of *h*BN-MoS₂-*h*BN heterostructures

Motivated by the theoretical prediction, we performed electrochemical lithium intercalation on *h*BN-MoS₂-*h*BN heterostructures in which several-layer-thick MoS₂ flakes were

sandwiched between exfoliated flakes of *h*BN (see Methods and Fig. 2a). The *h*BN-MoS₂-*h*BN heterostructure devices were integrated into electrochemical microreactors²⁰⁻²⁴ and intercalation was controlled potentiostatically by sweeping the electrochemical potential (V_{EC}) between the *h*BN-MoS₂-*h*BN working electrode and a lithium reference/counter electrode. Cr/Au metal contacts directly deposited onto the top surface of MoS₂ in the heterostructures served as the working electrode, while lithium metal pressed onto copper foil served as the reference/counter electrode (Fig. 2b). As V_{EC} is lowered from the open circuit voltage (O.C.), Li⁺ ions diffuse through the electrolyte and intercalate into the interlayer gaps of the heterostructure. We note that while multilayer MoS₂ flakes are used in experiments unlike the monolayer MoS₂ used in calculations, the computational predictions remain valid as they examine the binding energy of the MoS₂-*h*BN interface for 1T- and 2H-MoS₂, which we determined to be independent of increasing the thickness of MoS₂ up to two layers.

Intercalation dynamics of *h*BN-MoS₂-*h*BN heterostructures were compared to those of bare MoS₂ by sequentially lowering V_{EC} from O.C. (~2.5 V vs. Li/Li⁺) to 0.2 V vs. Li/Li⁺ at a decrement of 0.2 V. At each potential, V_{EC} was held constant for several minutes to acquire Raman spectra *in situ*, after which the samples were allowed to recover to O.C. before lowering V_{EC} to the next potential. *In situ* optical microscopy of a heterostructure during intercalation revealed that MoS₂ turned dark at 1.0 V vs. Li/Li⁺ (Fig. 2c), and bare MoS₂ also darkened at 1.0 V vs. Li/Li⁺ (Fig. 2d). The color change may indicate a phase transition to the 1T' phase²¹, and *in situ* Raman spectroscopy confirmed the 2H-1T' phase transition of MoS₂ in the heterostructure at 1.0 V vs. Li/Li⁺ and also in bare MoS₂ at 1.0 V vs. Li/Li⁺ (Fig. 2e). The phase transition from 2H- to 1T'-MoS₂ is clearly observed via the suppression of the characteristic E_{2g} and A_{1g} Raman modes of 2H-MoS₂ and the concurrent growth of the J₁ and J₂ modes of 1T'-MoS₂^{30,31}. We note that, due to

the low intensity of *h*BN Raman modes (Supplementary Fig. 2), we were unable to determine what effect lithium has on the structure of *h*BN. Supplementary Fig. 3 shows the full intercalation range of the heterostructure, including the transition to the amorphous state, which occurs at 0.4 V vs. Li/Li⁺, the same as in the bare MoS₂ case (Supplementary Fig. 4). Therefore, our key finding is that while encapsulating MoS₂ with *h*BN should theoretically significantly increase the thermodynamic stability of 1T'-MoS₂, it has no observable effect on the electrochemical voltage required to induce the 2H-1T' phase transition of lithium-intercalated *h*BN-MoS₂-*h*BN.

Lithium diffusion pathways in *h*BN-MoS₂-*h*BN heterostructures

One possible explanation for the lack of an observable difference between bare MoS₂ and *h*BN-MoS₂-*h*BN heterostructure is an increased Li⁺ diffusion pathway in the heterostructure. Li⁺ ions must diffuse over longer distances to access the MoS₂ flake in the heterostructure because the *h*BN flakes completely encase MoS₂ (Fig. 2a), such that Li⁺ ions in the electrolyte do not have direct access to the edges of the MoS₂ flake. To investigate this, we fabricated a *h*BN-MoS₂-*h*BN heterostructure and reactively ion-etched its perimeter, directly exposing the edges of MoS₂ to the liquid electrolyte while still covering the top and bottom surfaces of MoS₂ with *h*BN (Fig. 3a). Consistent with the results in Fig. 2, the 2H-1T' phase transition occurred at an applied V_{EC} of 1.0 V vs. Li/Li⁺ for the edge-exposed heterostructure, as shown by *in situ* Raman spectroscopy and optical microscopy (Fig. 3b and Supplementary Fig. 5). Further intercalation yielded amorphous MoS₂ at 0.4 V vs. Li/Li⁺ just as in the heterostructure without exposed edges. Therefore, despite Li⁺ ions having direct access to the edges of MoS₂, the edge-exposed *h*BN-MoS₂-*h*BN heterostructure still required a V_{EC} of 1.0 V vs. Li/Li⁺ to induce the 2H-1T' phase transition. Thus,

longer Li^+ diffusion pathways cannot explain the lack of observable difference in V_{EC} required for the phase transition in the heterostructure and bare MoS_2 .

To further investigate the effects of lithium diffusion pathways, we fabricated a $h\text{BN-MoS}_2-h\text{BN}$ heterostructure with the heterostructure edges completely covered with a thick layer of gold to block edge-intercalation (Fig. 3c)³². With this architecture, Li^+ ions could only reach MoS_2 through the basal planes of the top $h\text{BN}$ flake. *In situ* Raman spectra showed the onset of the 2H-1T' phase transition at an applied V_{EC} of 1.0 V vs. Li/Li^+ as shown by a mixture of both the A_{1g} and E_{2g} peaks of 2H- MoS_2 and the J_1 and J_2 peaks of 1T'- MoS_2 (Fig. 3d and Supplementary Fig. 6). The complete transition to 1T'- MoS_2 occurred at 0.8 V vs. Li/Li^+ , marked by the disappearance of the A_{1g} and E_{2g} peaks. In addition, *in situ* Raman spectra showed MoS_2 became amorphous after 15 minutes at a V_{EC} of 0.2 V vs. Li/Li^+ , instead of at the V_{EC} of 0.4 V vs. Li/Li^+ observed in the previous two heterostructures (Fig. 3a-b and Supplementary Figs. 3 and 5). Thus, our results from the edge-covered heterostructure show that, while $h\text{BN}$ is electrically insulating, it is ionically conductive, allowing Li^+ ions to diffuse through its basal planes. We attribute the ionic conductivity of the $h\text{BN}$ basal plane to intrinsic defects present in the commercially purchased $h\text{BN}$ crystals (Supplementary Fig. 2d), as pristine 2D $h\text{BN}$ crystals have been shown to be impermeable even to protons³³, but can become ionically conductive through intrinsic^{32,34} or engineered defects^{35,36}. The phase transitions in the edge-covered heterostructure were slightly delayed compared to the other two heterostructures, which is consistent with a previous report that suggests an increased energy barrier to lithium diffusion through the basal plane of bare MoS_2 as compared to through the interlayer gaps.³² Irrespective of the Li^+ diffusion pathways, all three $h\text{BN-MoS}_2-h\text{BN}$ heterostructures undergo the 2H-1T' phase transition at 1.0 V vs. Li/Li^+ , the same V_{EC} to induce the phase transition in bare MoS_2 . We thus show clearly that the presence of a $h\text{BN-}$

MoS₂ heterointerface does not allow for the 2H-1T' transition at a lower applied V_{EC} than bare MoS₂ in contrast to the prediction from DFT calculations.

Steric hindrance to the phase transition by *h*BN

Since our calculations indicate that the 1T-MoS₂-*h*BN interface is thermodynamically more stable than the 2H-MoS₂-*h*BN interface with Li intercalation, the lack of an observable difference in the 2H-1T' phase transition between bare MoS₂ and *h*BN-MoS₂-*h*BN suggests that there may be an additional energy barrier that influences the phase transition for the heterostructure. We conclude that steric hindrance from *h*BN at the heterointerface introduces an additional energy barrier to the nucleation of 1T'-MoS₂ at the interface, counteracting the thermodynamic stabilization of the 1T'-MoS₂-*h*BN interface. This is supported by the results from the edge-covered heterostructure (Fig. 3c), where the nucleation of the 1T' phase must be initiated at the top *h*BN-MoS₂ interface because the Li⁺ concentration is highest at the top *h*BN-MoS₂ interface as Li⁺ entered through the basal planes of the top *h*BN flake. The phase transition still occurred at 1.0 V vs. Li/Li⁺, suggesting an interface-induced barrier to the nucleation of the 1T' phase. We hypothesize that this energy barrier in *h*BN-MoS₂-*h*BN heterostructures is driven by sluggish kinetics due to the heterointerface. The phase transition requires atomic rearrangements of the sulfur atoms from a trigonal prismatic to an octahedral coordination surrounding the molybdenum atoms. This rearrangement is likely impeded by steric hindrance induced by the presence of the *h*BN layer in close proximity to the sulfur atoms, thus creating an activation energy barrier for the nucleation of the 1T' phase.

To test our hypothesis that there is an activation energy barrier for the 2H-1T' phase transition introduced by the *h*BN-MoS₂ interface, we investigated the phase transition of a *h*BN-MoS₂-*h*BN heterostructure as a function of both V_{EC} and temperature (Fig. 4). Increasing the temperature should lower the activation energy barrier and allow for the intercalation-induced phase transition to occur at a higher V_{EC} than the observed 1.0 V vs. Li/Li⁺ at room temperature. Initially at room temperature, *in situ* Raman spectroscopy showed that lowering V_{EC} to 1.1 V vs. Li/Li⁺ did not induce the phase change (Fig. 4b), consistent with the other heterostructures. After relaxing the device back to O.C., the microreactor was heated to 60 °C, and then V_{EC} was lowered to 1.1 V vs. Li/Li⁺. At 60 °C, *in situ* Raman indicated the device remained in the 2H phase (Fig. 4c); however, increasing the temperature to 100 °C for 5 minutes induced the transition to the 1T' phase at 1.1 V vs. Li/Li⁺, as shown by Raman spectroscopy and optical microscopy (Figs. 4c-d). Thus, the application of thermal energy reduced the applied electrochemical voltage by 0.1 V, suggesting it can overcome the energy barrier to the nucleation of the 1T' phase imposed by the heterointerface. Continued intercalation at 100 °C for an additional 15 minutes yielded amorphous MoS₂. Since the ionic conductivity of the liquid electrolyte at room temperature is already very high (10⁻³ S cm⁻¹)³⁷, we do not expect the application of thermal energy to significantly increase the intercalation of lithium, so the heating experiments further support the hypothesis that the MoS₂-*h*BN heterointerface introduces an activation energy barrier to the 2H-1T' phase transition due to steric hindrance.

We studied the role of the heterointerface in the phase stability and transition of a *h*BN-MoS₂-*h*BN heterostructure. We show that intercalation-induced phase changes can be manipulated via multi-modal control over applied electrochemical voltage, temperature, and heterointerfaces. While we show that *h*BN-MoS₂ interface did not show any observable differences in the

electrochemical energy required to induce the MoS₂ 2H-1T' phase transition, interfacing MoS₂ with other 2D materials may change the kinetics of the phase transition or modify the relative thermodynamic stabilities of 2H- and 1T'-MoS₂. This has broad implications for van der Waals heterostructured devices, in which heterointerfaces could modulate the kinetics of phase changes of 2D materials. Given the wide range of phases achievable in 2D materials,³⁸ our approach suggests opportunities to build devices with targeted electrochemical switching of material properties for a wide variety of applications.

Methods

Ab Initio Calculations:

The DFT calculations were carried out using the Quantum Espresso³⁹ package using a plane-wave basis set. Norm-converging pseudopotentials⁴⁰ were used to describe the valence electrons which included the semi-core 4s and 4p electrons of Mo, and the exchange-correlation was treated at the local density approximation⁴¹ (LDA) level, which produces excellent agreement with the experimental structure of bulk 2H and 1T MoS₂. The kinetic energy cut-off for the expansion of plane-waves was 2040 eV for all calculations.

We accounted for the effect of doping on the structure of the 2H and 1T MoS₂ by relaxing bulk 2H and 1T MoS₂ at various levels of implicit doping. The unit cell was allowed to relax until the energy was converged to within 0.02 meV/atom and the forces on atoms were smaller than 2.5×10^{-3} eV/Å. A Monkhorst-Pack⁴² shifted k-mesh of 42x42x8 was used for the calculations. The lattice parameters found in this relaxation were carried over to the calculations on the larger supercell with the heterointerface.

To model the heterointerface, we constructed supercells with one monolayer of 3x3 (2H- or 1T-) MoS₂ encapsulated in 6 layers of 4x4 hBN (Fig. 1b). We note that while the experiment is performed on few-layer MoS₂, the calculations are performed on monolayer MoS₂ to reduce computational cost. Increasing the number of MoS₂ layers to two does not change our reported results. In the supercell, the lattice parameters of 2H and 1T were constrained to the relaxed parameters of bulk MoS₂ (as described above). The stand-alone hBN was relaxed in the out-of-plane *c* direction while strained in the *a-b* plane (-4.78 % for 1H and -4.32% for 1T) to create a commensurate heterostructure. Then, the equilibrium distance between MoS₂ and hBN was

determined by minimizing the total energy as the distance between the MoS₂ and *h*BN was rigidly adjusted. To determine the binding energy of the MoS₂-*h*BN heterointerface, we then calculated the total energy of the supercell with the heterointerface ($E_{hetero.}$), as well as supercells with freestanding monolayer MoS₂ (E_{MoS_2}) and a 6-layer slab of *h*BN (E_{BN}^* , where * shows that the *h*BN was strained as described above) with 25 Å of vacuum. The binding energy is defined as,

$$\bar{E}_{bind} = \frac{E_{hetero.} - (E_{MoS_2} + E_{BN}^*)}{2 * A} \quad (1),$$

where A is the cross-sectional area of the heterointerface. We also tested a larger (less strained) supercell with a 4x4 (2H- or 1T-) MoS₂ and 5x5 *h*BN heterostructure consisting of 348 atoms. Since the reduced in-plane strain had little effect on the binding energies of the MoS₂-*h*BN interface (Supplementary Table 1), we used the 3x3 MoS₂-4x4 *h*BN supercell for the remaining calculations because it is computationally less expensive.

For the Li-doped heterostructures, a Li atom was placed over the Mo site, which is one of the most favored intercalation sites⁴³, and its separation from the Mo atom was systematically varied to locate the equilibrium position. With a Li atom included, the heterointerface binding energy is accordingly defined as

$$(\bar{E}_{bind,Li}) = \frac{E_{hetero.} - (E_{MoS_2} + E_{BN}^* + E_{Li})}{2 * A} \quad (2),$$

where E_{Li} is energy of an isolated Li atom in vacuum.

Heterostructure Assembly and Device Fabrication

MoS₂ (SPI Supplies) and *h*BN (HQ Graphene) flakes were mechanically exfoliated from bulk crystals onto SiO₂/Si substrates using the scotch-tape method. The substrates were sonicated in acetone and isopropyl alcohol, and treated with O₂ plasma prior to exfoliation. Flakes of desired size and thickness were transferred to dry thermal oxide SiO₂/Si substrates using a KOH-assisted technique, and MoS₂ and *h*BN flakes were stacked on each other to form *h*BN-MoS₂-*h*BN heterostructures as follows. A hemispherical droplet of epoxy (Scotch-Weld, Series DP100Plus) about 0.5 mm in diameter was cured on a glass slide. Then, a 13 wt. % solution of polypropylene carbonate (PPC, Sigma Aldrich) in anisole was spun coated onto the epoxy at 3000 RPM for 2 minutes and cured at 90 °C for 2 minutes. Using an optical microscope and a micro-manipulator that holds the glass slide, the epoxy/PPC droplet was positioned above a flake of interest and carefully lowered to contact the flake. About 30 μL of a 2M aqueous solution of potassium hydroxide (KOH, Sigma Aldrich) was added to the substrate to etch the top few Å of SiO₂, releasing the flake from the substrate onto the epoxy/PPC droplet (the portion of the glass slide in contact with the KOH was covered with a thin layer of epoxy to prevent etching of the glass). The glass slide with the epoxy/PPC/flake was then rinsed with deionized water to remove any KOH residue. Each flake was released from the glass slide by melting the PPC at 95-100 °C for 5 minutes while contacting a target substrate. The PPC was subsequently dissolved in chloroform overnight.

For electrochemical lithium intercalation, electrodes were patterned with electron beam lithography (Vistec Raith EBPG 5000+) and then 10 nm Cr / 100 nm Au was deposited using thermal evaporation (Mbraun EcoVap). For the heterostructure device with exposed edges, polymethyl methacrylate (PMMA) and hydrogen silsesquioxane (HSQ) were used as a mask for dry etching. First, a layer of PMMA A3 was spun coated on the heterostructure at 4000 RPM for

2 minutes and cured at 180 °C for 2 minutes. HSQ was subsequently spun coated at 3000 RPM with no baking. Electron beam lithography was used to pattern the PMMA/HSQ mask, which was developed in MF-312 developer (Rohm and Haas Electronic Materials) for 4 minutes. After developing, the device was rinsed in multiple DI-water baths in order to remove the developer. The finished mask protected the heterostructure, leaving only the edges exposed for reactive ion etching (Oxford Plasmalab 100). PMMA not covered by HSQ was first removed with O₂ plasma (20 sccm) under 50 W RF power for 15 seconds, exposing the edges. A mixture of O₂ (4 sccm) and CHF₃ (40 sccm) gases under 60 W RF power⁴⁴ for 2 minutes was used to etch the edges of the heterostructure. After etching, the PMMA/HSQ mask was removed with acetone.

Electrochemical Cell Fabrication

The electrochemical intercalation was performed directly on the heterostructure and bare MoS₂ devices. All devices fabricated on SiO₂/Si were attached to a glass slide, and the gold contacts of the devices were wire-bonded to copper tape for connection to electrical instrumentation. All subsequent steps were conducted in an argon glovebox.

For all *in situ* Raman experiments, intercalation was conducted with a liquid electrolyte using an enclosed cell that holds the device and electrolyte and is sealed with an optical-grade glass top cover^{20,21,32}. Three sides of the glass top cover were first sealed by epoxy, leaving one side open. After the epoxy was cured, a small piece (~3×3 mm) of lithium metal (0.38 mm-thick ribbon, Sigma-Aldrich) was pressed onto copper foil using a mechanical plier to ensure good contact. The lithium/copper foil was then inserted into the open side of the glass top cover. The liquid electrolyte, a battery-grade solution of 1 M lithium hexafluorophosphate in 50/50 v/v

ethylene carbonate / diethyl carbonate (LiPF₆ in EC/DEC, Sigma Aldrich), was added to the cell to submerge the device and lithium metal. The open side was then covered with epoxy and allowed to cure, forming an air-tight seal.

In Situ Raman Characterization During Intercalation

Intercalation cells were connected to a Biological SP300 potentiostat/galvanostat for the electrochemical intercalation of Li⁺. The Cr/Au contacts to the device served as the working electrode, while the lithium/copper served as the reference/counter electrode. Before intercalation, a Raman spectrum was taken at O.C. (typical O.C. values were 2.4 – 2.7 V vs. Li/Li⁺). Lithium was intercalated into the heterostructures potentiostatically by dropping V_{ec} vs. Li/Li⁺ at a scan rate of 10 mV s⁻¹. Upon reaching a desired V_{ec}, the cell was held at that potential while Raman spectra were collected. For multiple intercalation cycles, cells were allowed to recover to O.C. before the next intercalation. *In situ* heating experiments were conducted by placing the glass slide supporting the intercalation devices onto a hot-plate during intercalation.

All Raman spectra were taken with a Horiba LabRAM HR Evolution Spectrometer using a 633 nm HeNe laser with an 1800 lines/mm diffraction grating. Before intercalation, all samples were characterized at a laser power of ~3 mW to avoid damage, but after cell fabrication, a laser power of ~7.5 mW was used to increase the signal-to-noise ratio due to scattering by the electrolyte. *In situ* Raman spectra were collected with fifteen 5-second exposures.

References

1. Geim, A. K. & Grigorieva, I. V. Van der Waals heterostructures. *Nature* **499**, 419–425 (2013).
2. Novoselov, K. S., Mishchenko, A., Carvalho, A. & Castro Neto, A. H. 2D materials and van der Waals heterostructures. *Science* **353**, aac9439 (2016).
3. Cao, Y. *et al.* Unconventional superconductivity in magic-angle graphene superlattices. *Nature* **556**, 43–50 (2018).
4. Yankowitz, M. *et al.* Tuning superconductivity in twisted bilayer graphene. *Science* **363**, 1059–1064 (2019).
5. Finney, N. R. *et al.* Tunable crystal symmetry in graphene–boron nitride heterostructures with coexisting moiré superlattices. *Nat. Nanotechnol.* **14**, 1029–1034 (2019).
6. Kertesz, M. & Hoffmann, R. Octahedral vs. Trigonal-Prismatic Coordination and Clustering in Transition-Metal Dichalcogenides. *J. Am. Chem. Soc.* **106**, 3453–3460 (1984).
7. Dungey, K. E., Curtis, M. D. & Penner-Hahn, J. E. Structural Characterization and Thermal Stability of MoS₂ Intercalation Compounds. *Chem. Mater.* **10**, 2152–2161 (1998).
8. Wang, L., Xu, Z., Wang, W. & Bai, X. Atomic mechanism of dynamic electrochemical lithiation processes of MoS₂ nanosheets. *J. Am. Chem. Soc.* **136**, 6693–6697 (2014).
9. Dresselhaus, M. S. ed. *Intercalation in Layered Materials*. (Springer Science+Buisness Media LLC, 1986).
10. Eda, G. *et al.* Photoluminescence from chemically exfoliated MoS₂. *Nano Lett.* **11**, 5111–5116 (2011).

11. Chhowalla, M. *et al.* The chemistry of two-dimensional layered transition metal dichalcogenide nanosheets. *Nat. Chem.* **5**, 263–275 (2013).
12. Wan, J. *et al.* Tuning two-dimensional nanomaterials by intercalation: Materials, properties and applications. *Chem. Soc. Rev.* **45**, 6742–6765 (2016).
13. Lukowski, M. A. *et al.* Enhanced hydrogen evolution catalysis from chemically exfoliated metallic MoS₂ nanosheets. *J. Am. Chem. Soc.* **135**, 10274–10277 (2013).
14. Wang, H. *et al.* Electrochemical tuning of vertically aligned MoS₂ nanofilms and its application in improving hydrogen evolution reaction new reagents/analytic tools; H. *Proc. Natl. Acad. Sci.* **110**, 19701–19706 (2013).
15. Voiry, D. *et al.* The role of electronic coupling between substrate and 2D MoS₂ nanosheets in electrocatalytic production of hydrogen. *Nat. Mater.* **15**, 1003–1009 (2016).
16. Sood, A. *et al.* An electrochemical thermal transistor. *Nat. Commun.* **9**, 1–9 (2018).
17. Yazdani, S., Yarali, M. & Cha, J. J. Recent progress on in situ characterizations of electrochemically intercalated transition metal dichalcogenides. *Nano Res.* **12**, 2126–2139 (2019).
18. Zhou, X., Wan, L. J. & Guo, Y. G. Facile synthesis of MoS₂@CMK-3 nanocomposite as an improved anode material for lithium-ion batteries. *Nanoscale* **4**, 5868–5871 (2012).
19. Wang, H. *et al.* Electrochemical tuning of MoS₂ nanoparticles on three-dimensional substrate for efficient hydrogen evolution. *ACS Nano* **8**, 4940–4947 (2014).
20. Wan, J. *et al.* In situ investigations of Li-MoS₂ with planar batteries. *Adv. Energy Mater.* **5**, 1401742 (2015).
21. Xiong, F. *et al.* Li intercalation in MoS₂: in situ observation of its dynamics and tuning optical and electrical properties. *Nano Lett.* **15**, 6777–6784 (2015).

22. Kühne, M. *et al.* Ultrafast lithium diffusion in bilayer graphene. *Nat. Nanotechnol.* **12**, 895–900 (2017).
23. Bediako, D. K. *et al.* Heterointerface effects in the electrointercalation of van der Waals heterostructures. *Nature* **558**, 425–429 (2018).
24. Zhao, S. Y. F. *et al.* Controlled Electrochemical Intercalation of Graphene/h-BN van der Waals Heterostructures. *Nano Lett.* **18**, 460–466 (2018).
25. Zhou, Y. *et al.* Revealing the Contribution of Individual Factors to Hydrogen Evolution Reaction Catalytic Activity. *Adv. Mater.* **30**, 1706076 (2018).
26. Zhou, Y. *et al.* Unveiling the Interfacial Effects for Enhanced Hydrogen Evolution Reaction on MoS₂ /WTe₂ Hybrid Structures. *Small* **15**, 1900078 (2019).
27. Sun, L. *et al.* Layer-Dependent Chemically Induced Phase Transition of Two-Dimensional MoS₂. *Nano Lett.* **18**, 3435–3440 (2018).
28. Gao, G. *et al.* Charge Mediated Semiconducting-to-Metallic Phase Transition in Molybdenum Disulfide Monolayer and Hydrogen Evolution Reaction in New 1T' Phase. *J. Phys. Chem. C* **119**, 13124–13128 (2015).
29. Tang, W., Sanville, E. & Henkelman, G. A grid-based Bader analysis algorithm without lattice bias. *J. Phys. Condens. Matter* **21**, 084204 (2009).
30. Jiménez Sandoval, S., Yang, D., Frindt, R. F. & Irwin, J. C. Raman study and lattice dynamics of single molecular layers of MoS₂. *Phys. Rev. B* **44**, 3955–3962 (1991).
31. Kappera, R. *et al.* Phase-engineered low-resistance contacts for ultrathin MoS₂ transistors. *Nat. Mater.* **13**, (2014).
32. Zhang, J. *et al.* Reversible and selective ion intercalation through the top surface of few-layer MoS₂. *Nat. Commun.* **9**, 1–9 (2018).

33. Hu, S. *et al.* Proton transport through one-atom-thick crystals. *Nature* **516**, 227–230 (2014).
34. Caglar, M. *et al.* Tunable Anion-Selective Transport through Monolayer Graphene and Hexagonal Boron Nitride. *ACS Nano* **14**, 2729–2738 (2020).
35. Surwade, S. P. *et al.* Water desalination using nanoporous single-layer graphene. *Nat. Nanotechnol.* **10**, 459–464 (2015).
36. Rollings, R. C., Kuan, A. T. & Golovchenko, J. A. Ion selectivity of graphene nanopores. *Nat. Commun.* **7**, (2016).
37. Kufian, M. Z. & Majid, S. R. Performance of lithium-ion cells using 1 M LiPF₆ in EC/DEC (v/v = 1/2) electrolyte with ethyl propionate additive. *Ionics (Kiel)*. **16**, 409–416 (2010).
38. Yang, H., Kim, S. W., Chhowalla, M. & Lee, Y. H. Structural and quantum-state phase transition in van der Waals layered materials. *Nat. Phys.* **13**, 931–937 (2017).
39. Giannozzi, P. *et al.* QUANTUM ESPRESSO: A modular and open-source software project for quantum simulations of materials. *J. Phys. Condens. Matter* **21**, (2009).
40. Troullier, N. & Martins, J. L. Efficient pseudopotentials for plane-wave calculations. *Phys. Rev. B* **43**, 1993–2006 (1991).
41. Perdew, J. P. & Zunger, A. Self-interaction correction to density-functional approximations for many-electron systems. *Phys. Rev. B* **23**, 5048–5079 (1981).
42. Monkhorst, H. J. & Pack, J. D. Special points for Brillouin-zone integrations. *Phys. Rev. B* **13**, 5188–5192 (1976).
43. Nasr Esfahani, D., Leenaerts, O., Sahin, H., Partoens, B. & Peeters, F. M. Structural transitions in monolayer MoS₂ by lithium adsorption. *J. Phys. Chem. C* **119**, 10602–10609

(2015).

44. Wang, L. *et al.* One-dimensional electrical contact to a two-dimensional material. *Science* **342**, 614–617 (2013).

Acknowledgements

S.Y. acknowledges support from the Army Research Office (W911NF-18-1-0367) for device fabrication and intercalation experiments. J.V.P. was supported by the National Defense Science and Engineering Graduate (NDSEG) Fellowship Program, sponsored by the Air Force Research Laboratory (AFRL), the Office of Naval Research (ONR), and the Army Research Office (ARO). Device fabrication and characterization was carried out at the Yale Institute for Nanoscience and Quantum Engineering, the Yale West Campus Materials Characterization Core, the Yale West Campus Cleanroom, and the Yale School of Engineering & Applied Science Cleanroom. The calculations of the heterointerface used resources of the National Energy Research Scientific Computing Center (NERSC), a DOE Office of Science User Facility supported by the Office of Science of the U.S. Department of Energy under Contract No. DE-AC02-05CH11231; the Extreme Science and Engineering Discovery Environment (XSEDE), which is supported by National Science Foundation grant number ACI-1548562; and the Oak Ridge Leadership Computing Facility at the Oak Ridge National Laboratory, which is supported by the Office of Science of the U.S. Department of Energy under Contract No. DE-AC05-00OR22725. We thank the Yale Center for Research Computing use of the research computing infrastructure, specifically the Grace cluster, which was used for calculations on bulk MoS₂.

Author contributions

S.Y. and J.J.C. conceived the project. S.Y. carried out the experiments and analyzed data with assistance from J.V.P. *Ab initio* calculations were performed by A.K. and D.Y.Q. J.V.P., M.Y., J.M.W., and D.J.H. contributed to the development of experimental methods and characterization techniques. S.Y., J.V.P., and J.J.C. wrote the manuscript with input from all authors.

Competing interests

The authors declare no competing interests.

Additional information

Supplementary information is available for this manuscript.

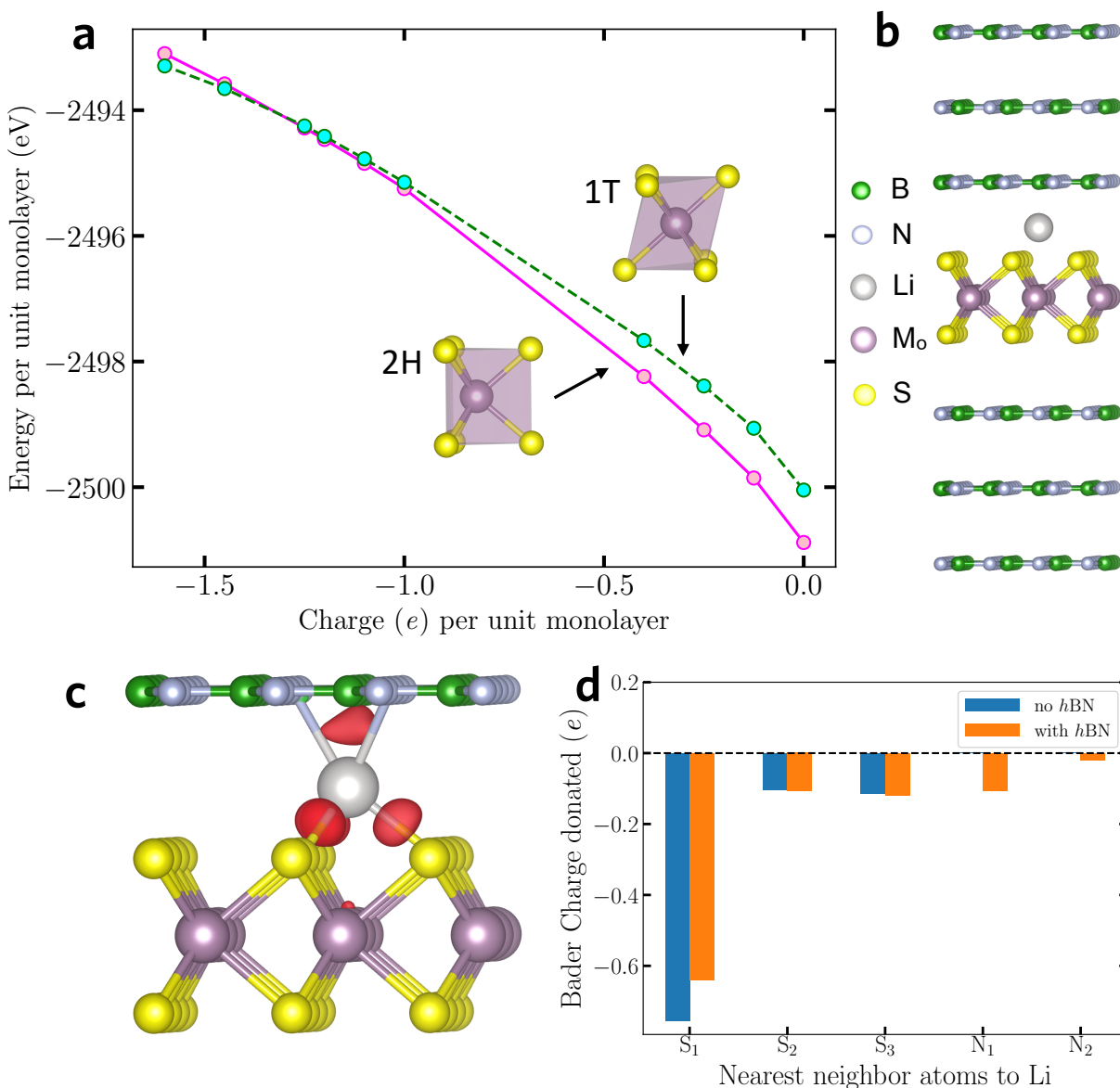


Fig. 1 | DFT Calculations of the 2H to 1T phase transition. **a** Total energy per monolayer of 1 unit cell of bulk MoS₂ as a function of added implicit charge for the 2H phase (pink) and the 1T phase (cyan). *Insets*, the trigonal prismatic coordination of sulfur atoms (yellow) around molybdenum (purple) in 2H-MoS₂ and their octahedral coordination in 1T-MoS₂. **b**. Supercell of the heterointerface with 6 layers of strained *h*BN, 1 layer of relaxed MoS₂, and 1 Li atom. **c**. Change in the charge density when Li is added to the heterointerface. Purple atoms are Mo, yellow are S, green are B, light blue are N, and the white atom is Li. Red represents the isosurface corresponding to 80% of the maximum charge density. **d**. Bader charge analysis of the charge donated by the Li atom to all its nearest neighbor S atoms (first nearest - S₁, 2nd nearest - S₂, and 3rd nearest - S₃) and its nearest N atoms (N₁ and N₂) with (orange) and without (blue) *h*BN encapsulation. The locations of S₁, S₂, S₃, N₁, and N₂ can be found in Supplementary Fig. 1.

Heterointerface	\bar{E}_{bind} (mJ/m ²)	$\bar{E}_{bind,Li}$ (mJ/m ²)
2H-MoS ₂ -hBN	-139	-378
1T-MoS ₂ -hBN	-142	-496

Table 1 | Binding energy of the 2H-MoS₂-hBN and 1T-MoS₂-hBN heterointerfaces with and without Li. The addition of Li increases the binding energy of the 1T-MoS₂-hBN heterointerface by 354 mJ/m² and the binding energy of the 2H-MoS₂-hBN interface by 239 mJ/m². Overall, the introduction of Li increases the binding energy of the 1T-MoS₂-hBN heterointerface relative to the 2H-MoS₂-hBN heterointerface by 118 mJ/m², whereas the binding energies are almost the same without Li.

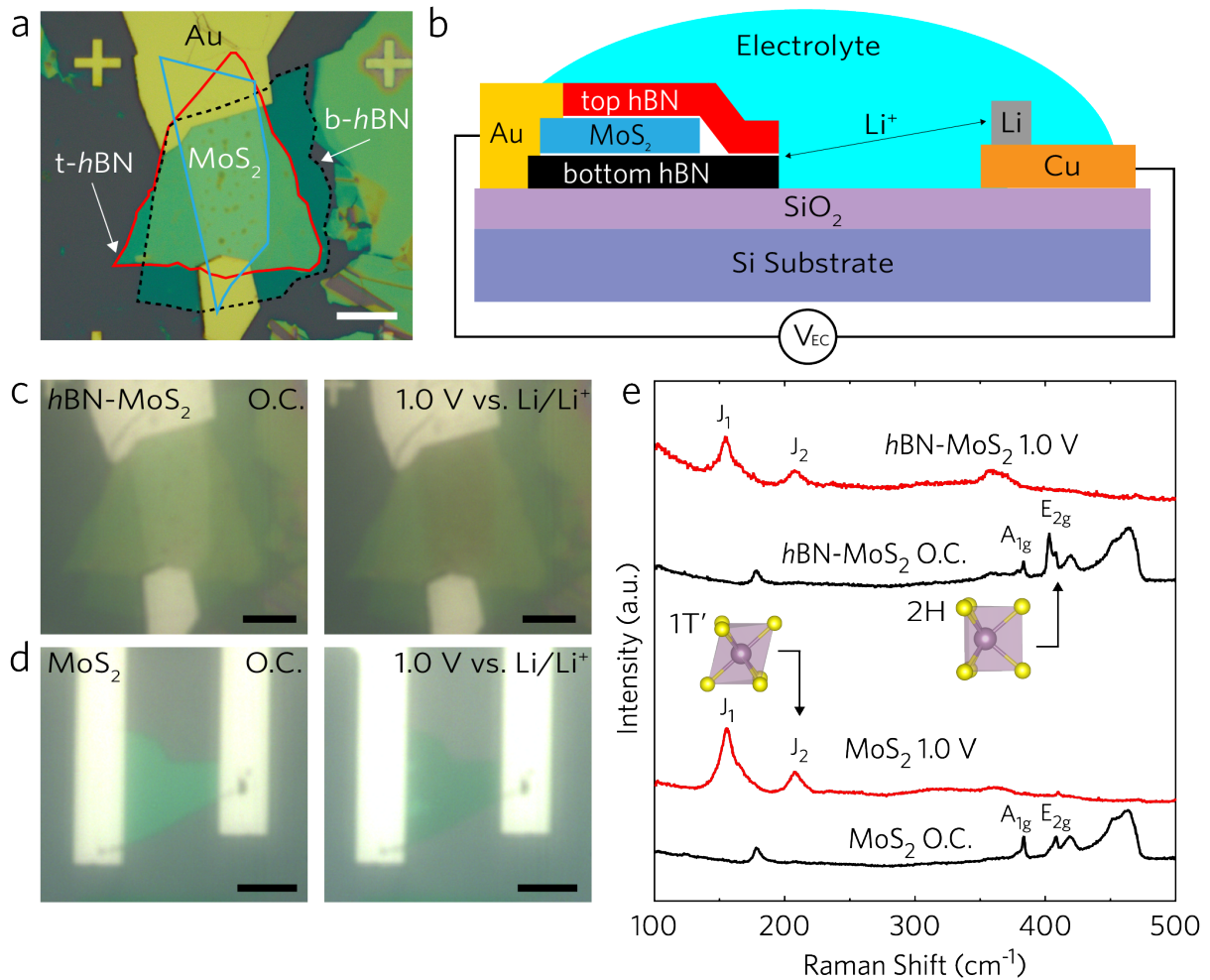


Fig. 2 | Li⁺ intercalation of *h*BN-MoS₂-*h*BN heterostructures. **a**, Optical micrograph of a *h*BN-MoS₂-*h*BN heterostructure with Cr/Au contacts to MoS₂, scale bar 10 μm. The MoS₂ flake (blue outline) is sandwiched between the top and bottom *h*BN flakes, denoted as *t-h*BN (red outline) and *b-h*BN (dashed-black outline), respectively. **b**, Schematic of an electrochemical microreactor for intercalating *h*BN-MoS₂-*h*BN. **c**, *In situ* optical micrographs of the heterostructure in (a) at open circuit (O.C.) and 1.0 V vs. Li/Li⁺, scale bars 10 μm. **d**, *In situ* optical micrographs of bare MoS₂ at O.C. and 1.0 V vs. Li/Li⁺, scale bars 10 μm. **e**, *In situ* Raman spectra of the devices shown in (c-d), with black and red indicating the 2H and 1T' phases, respectively. *Insets*, the trigonal prismatic coordination of sulfur atoms (yellow) around molybdenum (purple) in 2H-MoS₂ and their octahedral coordination in 1T'-MoS₂.

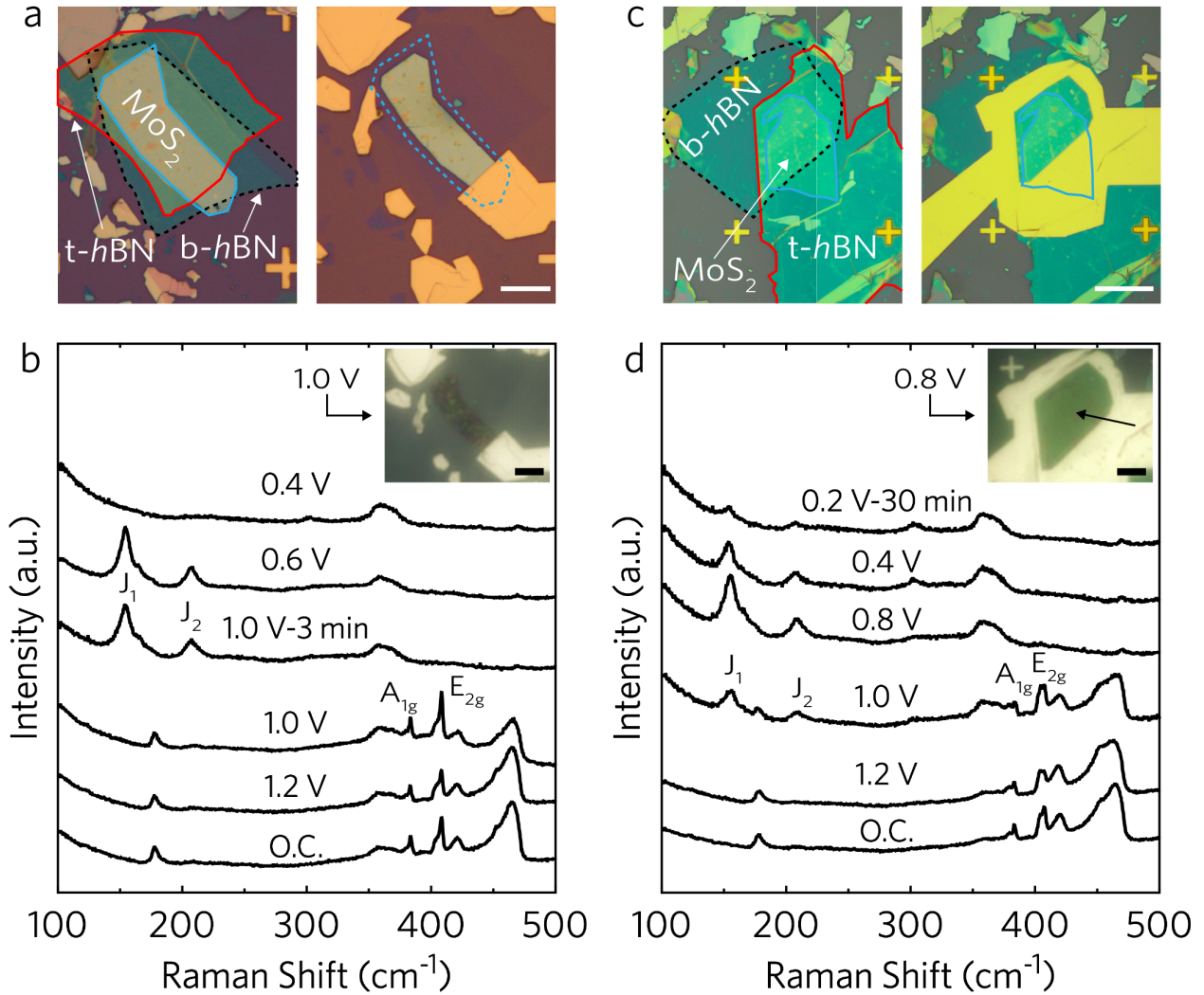


Fig. 3 | Different Li⁺ diffusion pathways during intercalation of hBN-MoS₂-hBN heterostructures. **a**, Optical micrographs of hBN-MoS₂-hBN before (left) and after (right) etching to expose the edges directly to liquid electrolyte, scale bar 10 μm. The blue-dashed line (right) indicates the original extent of MoS₂. **b**, *In situ* Raman spectra of the device in (a) while V_{EC} vs. Li/Li⁺ is lowered. *Inset*, optical micrograph of the device at 1.0 V vs. Li/Li⁺, scale bar 10 μm. **c**, Optical micrographs of hBN-MoS₂-hBN before (left) and after (right) covering the edges with gold, scale bar 10 μm. **d**, *In situ* Raman spectra of the device in (c) while V_{EC} vs. Li/Li⁺ is lowered. *Inset*, optical micrograph of the device at 0.8 V vs. Li/Li⁺ with a black arrow indicating the darkened region, scale bar 10 μm.

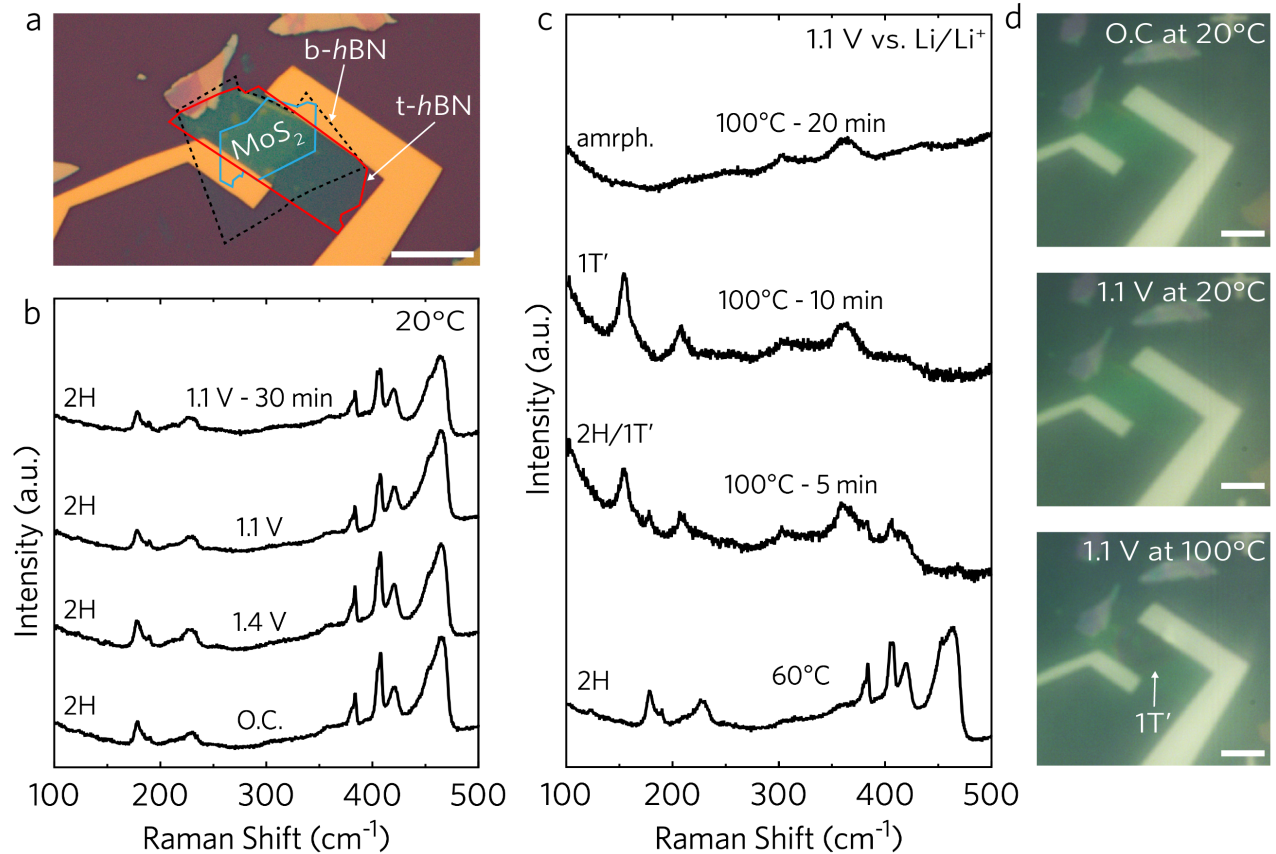


Fig. 4 | The 2H to 1T' phase transition in *h*BN-MoS₂-*h*BN as a function of temperature. **a**, Optical micrograph of the pristine heterostructure device, scale bar 10 μm. **b**, Raman spectra taken as V_{EC} is lowered vs. Li/Li⁺ at room temperature. **c**, Raman spectra taken at 1.1 V vs. Li/Li⁺ during heating. The onset of the 2H-1T' phase transition is observed after 5 minutes at 100°C, with a full transition to 1T'-MoS₂ after 10 minutes. The MoS₂ becomes amorphous after 20 minutes at 100°C. **d**, *In situ* optical micrographs taken at O.C., at 1.1 V vs. Li/Li⁺ at room temperature, and at 1.1 V vs. Li/Li⁺ at 100°C, scale bars 10 μm.